Mid- and Low-Latitude Ionospheric D Region Remote Sensing by Radio Atmospherics—Part I: Forward Modeling and Field Measurement Validations

Feng Han, *Member, IEEE*, Bingyang Liang, Jiawen Li, Feifan Liu, Gaopeng Lu, and Qing Huo Liu, *Fellow, IEEE*

***Abstract*— Radio atmospherics (sferics for short) are electromagnetic (EM) pulses discharged by lightning return strokes and can be used for D region remote sensing. A frequency-domain full-wave (FDFW) numerical model is developed to simulate sferics propagation in earth ionosphere waveguide (EIWG). For a certain sampling frequency, EM fields of sferics are decomposed into a series of plane waves in the spectral domain via 2-D spatial Fourier transforms. The magnetized cold plasma medium of ionosphere is divided into several thin layers with the arbitrary anisotropic dielectric constant for each layer. The EM fields at the sferics receiver site are evaluated by recursively computing the reflection and transmission matrices in all layer boundaries for all the plane wave components and performing 2-D numerical integration in the spectral domain. The earth flattening technique is adopted and the horizontal wave vector of each plane wave component is directly modified in the spectral domain to compensate for earth curvature effects. Interactions between plane waves and the magnetized cold plasma of ionosphere are analyzed and discussed. Comparisons between the FDFW computation and finite-difference time-domain simulation as well as field measured sferics are implemented to verify the accuracy and reliability of the proposed new model.**

***Index Terms*— Arbitrary anisotropic, D region remote sensing, earth flattening technique (EFT), ionosphere, magnetized cold plasma.**

I. Introduction

IONOSPHERE is one part of earth atmosphere and is composed of D, E, and F layers. It has significant effects on radio wave propagation since electromagnetic (EM) waves with different frequencies undergo reflection, refraction, absorption or attenuation inside the ionosphere. The D region exists around 60–90 km from ground and is difficult to measure. Because this altitude range is too high for balloons but too low for satellite measurements. Rocket *in situ* measurement is possible but the economical cost is high. Ionosonde cannot transmit low-frequency waves that can be reflected back by D region. Radio atmospherics (sferics for short) discharged by lightning return strokes have most energy concentrated in the very low frequency (VLF; 3–30 kHz) and extremely low frequency (ELF; 3–3000 Hz) bands [1], propagate in earth ionosphere waveguide (EIWG), and are bounced by the ground and the lower ionosphere (D region) but suffer from low attenuation [2]. Therefore, sferics become a useful tool for the D region remote sensing [1]. It is desirable to study the sferics propagation in EIWG to understand the remote sensing data.

There are two types of numerical models to simulate sferics propagation. One is performed in the time domain to compute the broadband waveforms at sferics receivers. The other one is to evaluate the amplitudes and phases for distinct frequencies at receiver locations. The finite-difference time-domain (FDTD) method is the most popular time-domain method. Since the ionosphere medium is plasma, the research work in this field began with the simulation of EM wave propagation in plasma. In [3], the dispersive property of ionospheric plasma was considered. However, the geomagnetic effect was not taken into account. The ionosphere was treated as isotropic cold plasma. Young [4] proposed a higher order FDTD model to obtain more accurate simulation results for EM wave propagation in cold plasma but the particle collisions were neglected. There are also several similar works dealing with wave propagation in plasma [5]–[9]. They are summarized and compared, and the details are given in [10]. In [11], both the particle collisions and the applied static magnetic field in plasma were considered, and the FDTD model was built for gyrotropic media. Since the geomagnetic field is not perpendicular to ground in most locations in earth, this article cannot be directly adopted to model EM wave propagation in the anisotropic EIWG. Cummer [12] reported a 2-D FDTD model that includes both the arbitrary anisotropy and particle

Manuscript received April 11, 2019; revised August 4, 2019; accepted September 14, 2019. Date of publication September 30, 2019; date of current version February 3, 2020. This work was supported by the National Natural Science Foundation of China under Grant 41504120. *(Corresponding authors: Gaopeng Lu; Qing Huo Liu.)*

F. Han, B. Liang, and J. Li are with the Fujian Provincial Key Laboratory of Electromagnetic Wave Science and Detection Technology, Xiamen University, Xiamen 361005, China, and also with the Institute of Electromagnetics and Acoustics, Xiamen University, Xiamen 361005, China (e-mail: feng.han@xmu.edu.cn).

F. Liu and G. Lu are with the School of Earth and Space Sciences, University of Science and Technology of China, Hefei 230026, China (e-mail: gplu@ustc.edu.cn).

Q. H. Liu is with the Department of Electrical and Computer Engineering, Duke University, Durham, NC 27708 USA (e-mail: qhliu@duke.edu).

Color versions of one or more of the figures in this article are available online at http://ieeexplore.ieee.org.

Digital Object Identifier 10.1109/TAP.2019.2943433

collisions of the ionosphere. However, it was assumed that the collision frequency was much higher than the wave frequency. This was later improved by Hu and Cummer [13]. The effects of all kinds of charged particles in the cold plasma of ionosphere were incorporated into the FDTD model by coupling the current equations derived from the Lorentz equation of all kinds of particle motions into Maxwell's equations. They compared the FDTD simulated results with field measured sferics and acquired a good match. The 2-D model developed in [13] was later extended to 3-D cases by Simpson's research group to account for more complex phenomenon in magnetized clod plasma such as Faraday rotation [14] and the global EM wave propagation in the subionosphere environment [15]. More complicated FDTD models also include the variability (or uncertainty) of the ionosphere [16], [17]. However, in all the FDTD models mentioned above, the computation domain is fixed. In [18] and [19], a moving domain is proposed to save the computation time which is useful for a long propagation distance. Bérenger [20], [21] later also presented the postprocessing technique to remove the numerical dispersion and the implicit scheme to further accelerate the FDTD simulation of VLF wave propagation inside EIWG. Besides the aforementioned models, there are additional FDTD models dealing with local ionosphere perturbations associated with lightning discharges [22], [23].

On the other hand, the frequency domain model has been widely applied to the calculation of global VLF subionospheric propagation. The most famous frequency domain model is the long wave propagation capability (LWPC) which was developed by the Naval Ocean Systems Center [24]. LWPC is based on waveguide mode theory [25] and thus has a mode finder. The EM fields at the receivers are the superposition of a series of independently propagating wave modes in EIWG. The original LWPC model can only be used to evaluate the horizontal magnetic fields on the ground excited by vertical electric dipoles placed near the ground. This issue was later addressed by Pappert and Ferguson [26] using high gain functions. LWPC has been successfully applied to modeling the sferics propagation in EIWG by computing the signal spectra over wide ranges of frequencies [27]. Compared with the FDTD model, LWPC has no numerical dispersion but achieves the same accurate results as FDTD calculation [28].

In this article, we developed a new frequency-domain full-wave (FDFW) model to simulate sferics propagation in EIWG. For a time-harmonic wave with a certain frequency excited by the lightning current source, it is decomposed into a series of plane waves in the spectral domain through 2-D Fourier transforms. The ionospheric D region is divided into several subwavelength thin layers with the arbitrary anisotropic dielectric constant in each layer. Reflection and transmission coefficients of each plane wave component in all layer boundaries are derived. The EM fields at sferics receivers are acquired by 2-D integration in the spectral domain. In FDFW model, the anisotropy of the magnetized cold plasma of ionosphere is directly manifested in the medium dielectric constant. This is quite different from most previous FDTD models [12]–[21]. Because the anisotropy of the cold plasma caused by motions of charged particles subject to the ambient geomagnetic field is taken into account in the FDTD model by coupling the Lorentz current equations into Maxwell's equations instead of modifying the medium dielectric constants, they remain the same as those for the free space. Our model is also different from LWPC. In LWPC, the auxiliary Hertz vector and image theory are used. The measured EM fields are the summation of a series of discrete modes which can survive in EIWG and propagate to receivers before being completely attenuated. Therefore, the mode finder is very important in LWPC. In our model, the EM fields at the receivers are the continuous integration in the spectral domain. All the modes including traveling waves, evanescent waves, surface waves or other modes are included. This enables the direct observation of interactions between EM waves and the cold plasma medium of ionosphere at high altitudes.

The motivation for developing the FDFW model is to combine it with an inverse model to reconstruct the anisotropic dielectric parameters of each discretized layer of the ionospheric D region in the future, which will be part II of our research. It should be noted that an iterative inverse model always calls a forward model several times to obtain the unknown model parameters. In our previous work [29], we have successfully reconstructed the underground conductivity in each discretized layer using the iterative inversion. Although the FDTD is also a forward computation model and can be used to evaluate the broadband sferics at the receivers efficiently, it is not convenient to combine it with a frequency domain inverse model since the anisotropic dielectric parameters of ionosphere are not explicitly included in the FDTD model. Their effects are actually manifested by coupling the Lorentz current equations into Maxwell's equations. Similarly, although the LWPC is a frequency domain model, it is based on waveguide mode theory, and thus is also not easily used to construct the cost function of the inverse model since the ionosphere anisotropic parameters in all discretized layers must be explicitly combined together to form a vector in the inverse model [29]. The organization of this article is as follows. In Section II, the theories, methods, and techniques for the computation of sferics spectra which are affected by the magnetized cold plasma of ionosphere are described. The fast computation of EM fields excited by a line source is presented. The application of earth flattening technique (EFT) to compensate earth curvature effects is discussed. In Section III, numerical computation results are presented and discussed, and comparisons between FDFW model and FDTD simulations are performed to verify the accuracy. In Section IV, field measured data are used to verify the simulated sferics by FDFW model. In Section V, conclusions are drawn and discussions are presented. Finally, it should be noted that the time dependence $e^{j\omega t}$ will be used throughout this article.

II. Theories, Methods, and Techniques

In this section, we will discuss the dielectric constant of magnetized cold plasma of ionosphere, the wavefield evaluation in a layered medium by plane wave decomposition, computation of EM fields excited by the lightning line source as well as the compensation for earth curvature effects.

A. Anisotropic Dielectric Constants of Ionosphere

Ionosphere exists in the plasma state and includes all kinds of charged particles. Among them, electrons have the dominant effects on radio wave propagation since ions are much heavier than electrons. In most ELF/VLF frequency range, the ion effects can be neglected. Only when the EM wave frequency is lower than 150 Hz and close to the ion cyclotron frequencies or the altitude is higher than 110 km can the ions take notable effects [13]. In this article, we focus on the frequency range of sferics between 500 Hz and 30 kHz and D region below 100 km since most energy of sferics distributes in this range, and is reflected back by ionosphere below 100 km. Therefore, two important physical variables used to depict the ionospheric D region are electron density and electron collision frequency. In most literatures, they are modeled varying exponentially with altitude. The widely used electron density and collision frequency profiles are given as [30]

$$N_e(z) = 1.43 \times 10^{13} \exp(-0.15h') \times \exp[(\beta - 0.15)(z - h')] \ \mathrm{m}^{-3} \tag{1a}$$

$$\nu_e(z) = 1.816 \times 10^{11} \exp(-0.15z) \ \mathrm{s}^{-1} \tag{1b}$$

where z is the altitude relative to the ground surface with the unit km. The parameter h' is the altitude of the whole exponential profile with the unit km, while β represents the profile sharpness with the unit km^{-1}. Larger h' means a higher profile or smaller electron density at a fixed altitude. Larger β implies that the electron density increases faster with altitude increment. The profiles given in (1) have been used to verify the sferics propagation in EIWG in a lot of previous work [1], [13]. They will also be used to verify our model in this article. Although the true ionospheric D region profile may be not exactly the same as (1) [31], we do not comment much on this in this article. In addition, it should be noted that ionosphere varies with time. But the time scale of sferics propagation in EIWG is much smaller than that of ionosphere variation. D region also varies with spatial locations. For example, intense lightning discharges can modify the lower ionosphere and thus causes local electron density perturbations [32]. However, this exceeds the scope of this article. We only deal with the static ionosphere, i.e., we assume the electron density and collision frequency only vary with altitude, do not change with time, and have no horizontal gradient. The issue of perturbed ionosphere will be addressed in our future work.

Three physical variables used to describe the plasma state of ionosphere are plasma frequency ω_p, electron collision frequency ν_e, and electron cyclotron frequency ω_c. The ω_p is determined by N_e and ω_c is related to ambient geomagnetic field $\mathbf{B}_0$. These three variables also vary with altitude and are functions of z. For brevity, we omit z in the following derivation. The plasma frequency ω_p is defined as

$$\omega_p = \sqrt{\frac{N_e e^2}{m_e \epsilon_0}} \simeq 56.4\sqrt{N_e} \tag{2}$$

where N_e has the unit m^{-3}, m_e is the electron mass, e is the electron charge with the positive sign, and ϵ_0 is the permittivity of free space. The cyclotron frequency ω_c is defined as

$$\omega_c = \frac{eB_0}{m_e} \tag{3}$$

where B_0 is the geomagnetic field value. As shown in Fig. 1, B_0 is positive when $\mathbf{B}_0$ aligns with the positive $\hat{z}'$-axis. The complex permittivity of the gyrotropic ionosphere plasma in local coordinate $\hat{x}'\hat{y}'\hat{z}'$ is written as

$$\overline{\overline{\varepsilon}}' = \begin{bmatrix} \varepsilon_1 & j\varepsilon_2 & 0 \\ -j\varepsilon_2 & \varepsilon_1 & 0 \\ 0 & 0 & \varepsilon_3 \end{bmatrix} \tag{4}$$

where $\hat{z}'$ is parallel to the local geomagnetic field direction, and

$$\varepsilon_1 = \varepsilon_0 \left[1 - \frac{\omega_p^2 \left(1 - j\frac{\nu_e}{\omega}\right)}{(\omega - j\nu_e)^2 - \omega_c^2} \right] \tag{5a}$$

$$\varepsilon_2 = \varepsilon_0 \left[\frac{-\omega_c \omega_p^2}{\omega((\omega - j\nu_e)^2 - \omega_c^2)} \right] \tag{5b}$$

$$\varepsilon_3 = \varepsilon_0 \left[1 - \frac{\omega_p^2}{\omega(\omega - j\nu_e)} \right]. \tag{5c}$$

In above three equations, ω is the angular frequency of EM wave. In most locations in earth, the geomagnetic field $\mathbf{B}_0$ is not perpendicular to ground. However, it is convenient to define the $\hat{z}$-axis perpendicular to ground in the FDFW model. Therefore, a coordinate rotation is necessary to acquire the new permittivity. As shown in Fig. 1, we define the new global coordinate $\hat{x}\hat{y}\hat{z}$ with $\hat{z}$ pointing upward and $\hat{x}$ pointing to the geographic east. The $\hat{x}'$-axis lies inside the horizontal $\hat{x}\hat{y}$ plane. The angle between geographic north and geomagnetic north is the declination θ_d. It is positive when geomagnetic north is to the east of geographic north but negative otherwise. The angle between geomagnetic field $\mathbf{B}_0$ and geomagnetic north is the inclination θ_i. It is positive when $\mathbf{B}_0$ points downward but negative otherwise. It is not difficult to obtain the permittivity in the user-defined global coordinate $\hat{x}\hat{y}\hat{z}$ by rotation

$$\overline{\overline{\varepsilon}} = \mathbf{Q}\,\overline{\overline{\varepsilon}}'\,\mathbf{Q}^T \tag{6}$$

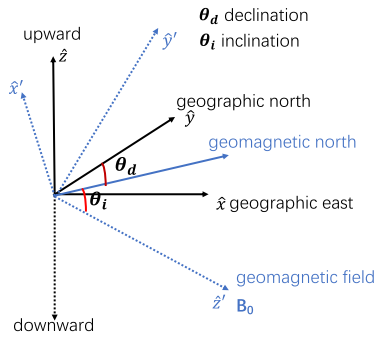

Fig. 1. Illustration of the coordinate rotation. In the local coordinate system $\hat{x}'\hat{y}'\hat{z}'$, $\mathbf{B}_0$ is aligned with the positive $\hat{z}'$-axis. In the user-defined global coordinate system $\hat{x}\hat{y}\hat{z}$, $\hat{z}$-axis is pointing upward and perpendicular to ground, and $\hat{x}$-axis points to geographic east.

where T denotes the matrix transpose and $\mathbf{Q}$ is the rotation matrix given as

$$\mathbf{Q} = \begin{bmatrix} -\cos\theta_d & \sin\theta_i\sin\theta_d & \cos\theta_i\sin\theta_d \\ \sin\theta_d & \sin\theta_i\cos\theta_d & \cos\theta_i\cos\theta_d \\ 0 & \cos\theta_i & -\sin\theta_i \end{bmatrix}. \tag{7}$$

Obviously, in the user-defined global coordinate $\hat{x}\hat{y}\hat{z}$, the permittivity of magnetized cold plasma of ionosphere becomes arbitrary anisotropic.

B. Wavefields Evaluation in the Planarly Layered Anisotropic Cold Plasma of Ionosphere

Suppose the ionosphere is divided into several planarly thin layers and an electric dipole is positioned inside one layer. Since the permittivity $\overline{\overline{\varepsilon}}$ only varies in the $\hat{z}$-direction and the $\hat{x}\hat{y}$ plane is infinitely large, the EM field excited by the dipole can be decomposed into a series of plane waves by 2-D Fourier transforms

$$\mathbf{E}(\mathbf{r}) = \iint_{-\infty}^{+\infty} \tilde{\mathbf{E}}(\mathbf{k}_s, z)\exp(-j\mathbf{k}_s\cdot\boldsymbol{\rho})dk_x dk_y \tag{8a}$$

$$\mathbf{H}(\mathbf{r}) = \iint_{-\infty}^{+\infty} \tilde{\mathbf{H}}(\mathbf{k}_s, z)\exp(-j\mathbf{k}_s\cdot\boldsymbol{\rho})dk_x dk_y \tag{8b}$$

where $\mathbf{r} = \hat{x}x + \hat{y}y + \hat{z}z$ is the spatial position of the field point, $\mathbf{k}_s = \hat{x}k_x + \hat{y}k_y$ is the wave vector in the horizontal plane, $\boldsymbol{\rho} = \hat{x}(x - x') + \hat{y}(y - y')$ is the horizontal vector pointing from the source point (x', y', z') to the field point (x, y, z), and $\tilde{\mathbf{E}}$ and $\tilde{\mathbf{H}}$ are the complex field amplitudes in the spectral domain. The integrands in (8) represent plane wave components. An auxiliary vector $\boldsymbol{\varphi}(k_x, k_y, z)$ can be defined and complete spectral-domain plane wave expressions are obtained by matching the wave amplitudes at the singular plane $z = z'$. Here z denotes the position at which the field point is locating while z' denotes the position at which the dipole source is locating. The detailed procedure for wavefield decomposition in an arbitrary anisotropic medium can be found in [33].

When an EM wave enters an anisotropic medium, it is split into two waves. They are called type I and type II waves. In literature, they are sometimes also referred as ordinary and extraordinary waves or transverse electric (TE) and transverse magnetic (TM) waves. Type I and type II waves are generated by two eigenvalues solved from the state equation matrix [33]. Therefore, in mathematics, it is not easy to distinguish them. In a layered arbitrary anisotropic medium, the reflection and transmission coefficients are matrices since there is a cross coupling between type I and type II waves. For the upgoing and downgoing waves in a layer boundary, they are, respectively, defined as

$$\mathbf{R}^u = \begin{bmatrix} R^u_{11} & R^u_{12} \\ R^u_{21} & R^u_{22} \end{bmatrix} \qquad \mathbf{R}^d = \begin{bmatrix} R^d_{11} & R^d_{12} \\ R^d_{21} & R^d_{22} \end{bmatrix} \tag{9a}$$

$$\mathbf{T}^u = \begin{bmatrix} T^u_{11} & T^u_{12} \\ T^u_{21} & T^u_{22} \end{bmatrix} \qquad \mathbf{T}^d = \begin{bmatrix} T^d_{11} & T^d_{12} \\ T^d_{21} & T^d_{22} \end{bmatrix}. \tag{9b}$$

These four coefficient matrices, $\mathbf{R}^u$, $\mathbf{R}^d$, $\mathbf{T}^u$, and $\mathbf{T}^d$, can be obtained by matching the tangential components of the wavefields in the boundary of two adjacent arbitrary anisotropic layers. The detailed derivations are presented in [33] and will not be repeated here. The off-diagonal elements of these four matrices become zero when the arbitrary anisotropic medium degenerates into a uniaxial anisotropic medium. Once the reflection and transmission matrices in (9) are computed for all layer boundaries, the global reflection matrices can be obtained in a recursive way [33]. The spectral domain complex plane wave amplitudes in the integrands of (8) at the field point $\mathbf{r}$ are acquired, and the 2-D numerical integration of k_x and k_y in (8) are performed to evaluate the field values in the spatial domain.

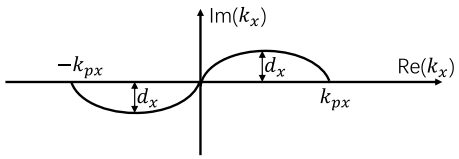

Fig. 2. Deformed integration path in the complex k_x-plane.

In this article, the 2-D integration path in (8) is different from that adopted in [33]. When the layered medium is highly conductive, the poles and branch cuts are far away from the real k_x-k_y plane, and the 2-D integration can be carried out along the real k_x- and k_y-axes. However, for sferics propagation in EIWG, the air (below ~60 km) is lossless although both the ground and ionosphere are highly conductive for ELF/VLF waves. Therefore, we deform the integration path to the complex k-plane to avoid the critical points, as shown in Fig. 2. The arc path between $-k_{px}$ and k_{px} complies with a sinusoid function. The parameter k_{px} is chosen as $1.5k_{max}$ where k_{max} is determined by the maximum wavenumber for all layers. The selection of d_x is discussed in [34]. For the integration of k_y in (8), the same path deformation applies.

In addition, for sferics propagation, the distance between the lightning source and the receiver is always several hundred kilometers. This large distance makes the integrands in (8) highly oscillatory in the k_x-k_y space. Therefore, the integration along the arc segment between $-k_{px}$ and k_{px} shown in Fig. 2 is accomplished by using Gauss quadrature. But for the line segments $(-\infty, -k_{px})$ and (k_{px}, ∞), iterative Aitken transformation is employed [35]. Although the method presented in [35] is for Sommerfeld type integration, it is straightforward to apply it to 2-D integration for k_x and k_y.

C. EM Wavefields Excited by the Line Source for the Lightning Current Channel

In nature, there are two types of lightning strokes. One is the could to ground (CG) lightning return stroke. It occurs between a thundercloud and the ground and its current channel is always almost vertical to ground. The other is the intracloud (IC) lightning stroke which always occurs between two thunderclouds. Its lightning current channel is oblique.

The lightning current channel is approximated as a line source. The numerical models for the lightning stroke current are usually complicated. One commonly used current moment model for the CG lightning is the doubly exponential expression [36]

$$I_m(t) = I_0\frac{\nu_0}{\gamma}[e^{-at} - e^{-bt}][1 - e^{-\gamma t}] \quad \text{A}\cdot\text{m} \tag{10}$$

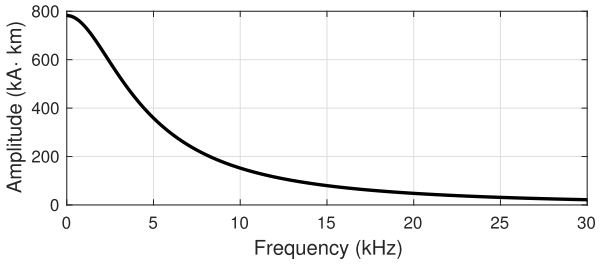

Fig. 3. Spectrum of the current moment of a lightning return stroke.

where $I_0 = 2 \times 10^4$ A, $\nu_0 = 8 \times 10^7$m/s, $\gamma = 3 \times 10^4$/s, $a = 2 \times 10^4$/s, $b = 2 \times 10^5$/s [37]. Fig. 3 shows the spectrum of $I_m(t)$. Most energy of such a current waveform concentrates in the ELF/VLF ranges.

In order to compute the EM waves excited by a CG lightning return stroke, we divide the vertical line current channel into several segments with the length of each segment far less than the wavelength. Each segment is approximated as a vertical polarized electric dipole. The field values at the receivers are the summation of EM fields excited by all the vertical electric dipoles. As shown in (8), the 2-D Fourier transforms are implemented in the horizontal plane, and the factor $\exp(-j\mathbf{k}_s \cdot \boldsymbol{\rho})$ in the integrand is the same for all the vertical dipoles. Therefore, we can accomplish the summation of $\tilde{\mathbf{E}}$ and $\tilde{\mathbf{H}}$ in the spectral domain for all the dipoles and then perform the integration. In addition, the reflection and transmission matrices in (9) only need computing once for all the vertical dipoles. These comments suggest that compared with the evaluation of EM fields excited by a dipole source, the computation cost of EM fields excited by a vertical lightning current channel does not increase too much.

However, this advantage is lost for an IC lightning stroke because the current channel is oblique. The factor $\exp(-j\mathbf{k}_s \cdot \boldsymbol{\rho})$ in the integrand is different for different dipoles. Therefore, the summation can only be carried out after the integration performed for different dipoles. This increases the computation cost. The EM waves discharged by an IC lightning stroke have the most energy distributed in high-frequency bands, from tens of mega-hertz to hundreds of mega-hertz [38]. Therefore, they have a short propagation distance and cannot be used for ionosphere remote sensing. We will not consider the computation of wavefields generated by IC lightning discharges in this article.

D. Compensation for Earth Curvature Effects in the Spectral Domain

In the above discussion, we assume the ionosphere is divided into a series of planarly thin layers. However, when the sferics propagation distance is long, e.g., more than 500 km or even approaching 1000 km, earth curvature cannot be neglected. Under this condition, spherical layers are appropriate for computation. But direct computation of wavefields in an anisotropic spherically layered medium is complicated [39]. One approximate solution is to map the ray tracing path in a spherically layered medium to a planarly layered medium. This method is called the EFT [40].

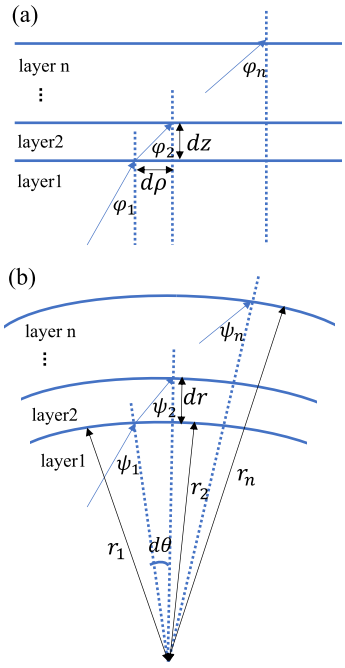

Fig. 4. Ray tracing schematics in layered media. (a) Planarly layered medium. (b) Spherically layered medium.

First, let us assume the layered medium is isotropic. As shown in Fig. 4, a plane wave impinges on the top boundary of layer 1 with the incident angle φ_1 or ψ_1 and it has the refraction angle φ_2 or ψ_2 in layer 2. Similar refractions occur in all layer boundaries, and thus the ray gradually bends down since the permittivity gradually decreases as the altitude increases in the ionosphere. This is the sferics refraction process in the upper boundary of EIWG. Based on the configuration shown in Fig. 4, it is not difficult to obtain

$$\sqrt{\varepsilon_1}\sin\varphi_1 = \sqrt{\varepsilon_2}\sin\varphi_2 = \cdots \sqrt{\varepsilon_n}\sin\varphi_n \tag{11a}$$

$$r_1\sqrt{\varepsilon_1}\sin\psi_1 = r_2\sqrt{\varepsilon_2}\sin\psi_2 = \cdots r_n\sqrt{\varepsilon_n}\sin\psi_n \tag{11b}$$

where ε_n is the permittivity of nth layer. Equation (11a) is the Snell law and only valid for a planarly layered medium. For a spherically layered medium, (11b) is used to replace (11a). It is called Bouger law and its proof is straightforward [40].

Let us choose r_1 as the reference point and assume the incident angles $\varphi_1 = \psi_1$ in layer 1. Equation (11b) can be manipulated as

$$\sqrt{\varepsilon_1}\sin\psi_1 = \frac{r_2}{r_1}\sqrt{\varepsilon_2}\sin\psi_2 = \cdots \frac{r_n}{r_1}\sqrt{\varepsilon_n}\sin\psi_n. \tag{12}$$

Equations (11a) and (12) have the same form if we replace $(r_2/r_1)\sqrt{\varepsilon_2}$ with $\sqrt{\varepsilon_2}$, …, $(r_n/r_1)\sqrt{\varepsilon_n}$ with $\sqrt{\varepsilon_n}$. This is to say, the ray tracing in a spherically layered medium is the same as that in a planarly layered medium if we scale the refractive index in each layer of a spherically layered medium by $(r_2/r_1), \ldots, (r_n/r_1)$. It looks like that earth surface is flattened by the modified refractive index.

Equation (11b) can be manipulated in another way as

$$\frac{r_1}{r_2}\sqrt{\varepsilon_1}\sin\psi_1 = \sqrt{\varepsilon_2}\sin\psi_2, \ldots, \frac{r_1}{r_n}\sqrt{\varepsilon_1}\sin\psi_1 = \sqrt{\varepsilon_n}\sin\psi_n. \tag{13}$$

Equation (11a) is also the phase matching condition and implies that the horizontal wave vector $\mathbf{k}_s$ is the same in all planar layers. By comparing (13) with (11a), we can easily come to another solution of EFT, i.e., scaling $\mathbf{k}_s$ in layer 1 by (r_1/r_2), ..., (r_1/r_n) and treat them as the horizontal wave vector in layer 2, ... layer n, respectively. Since the phase matching condition also holds for an anisotropic planarly layered medium, it is convenient to use the modified horizontal wave vector in our model. We choose a reference point, e.g., near earth surface, and modify $\mathbf{k}_s$ in all other layers before computing the reflection and transmission matrices and perform the integration in (8). The application of modified $\mathbf{k}_s$ for EFT in an anisotropic spherically layered medium has been discussed in [40].

At last, we want to emphasize that the EFT used in our model is different from previous work. In [13], the EFT is realized by the modified refractive index. In [15], irregular discretized cells such as trapezoidal cells or triangular cells are used to account for the earth curvature.

III. Numerical Results

In this section, we run the newly built FDFW model and discuss the numerical results. Both plane waves and sferics excited by a lightning return stroke are modeled and the results are discussed or compared with FDTD results from literatures.

A. Plane Waves Impinge on Ionosphere

Although EM waves excited by a lightning return stroke have high power and can be used for D region remote sensing, their interactions with magnetized cold plasma of ionosphere are complicated. In order to explore the interaction mechanisms, we first consider a plane wave incidence. Several assumptions and simplifications are made.

1) We choose the D region electron density and collision frequency profiles given in (1), and let $h' = 85$ km and $\beta = 0.5$ km^{-1}. This is a typical nighttime D region electron density profile [41].
2) We study the ionosphere in northern hemisphere, and assume the inclination θ_i is 45°.
3) The plane wave obliquely impinges on the ionosphere bottom with an incident angle of 45°.
4) The reflection of ground is omitted. Only the upgoing waves at different altitudes are studied. The downgoing waves are temporarily excluded in the computation. Because the wavefields at different altitudes are the summation of upgoing waves and downgoing waves, detaching the upgoing waves helps us more easily understand the effects of ionosphere on EM waves propagating inside it.
5) With respect to the plane of incidence (POI), only the TM polarization is included in the incident wave. This is consistent with the radio sferics polarization since the lightning return stroke is vertically polarized current. In the simulation, we assume the amplitude of the TM wave is 1 V/m.

Fig. 5 shows the variations of reflection and transmission coefficients of the upgoing wave at different altitudes of ionosphere. We choose two frequencies, 1 and 20 kHz in the ELF/VLF bands for simulation. Several observations are made from the simulated results.

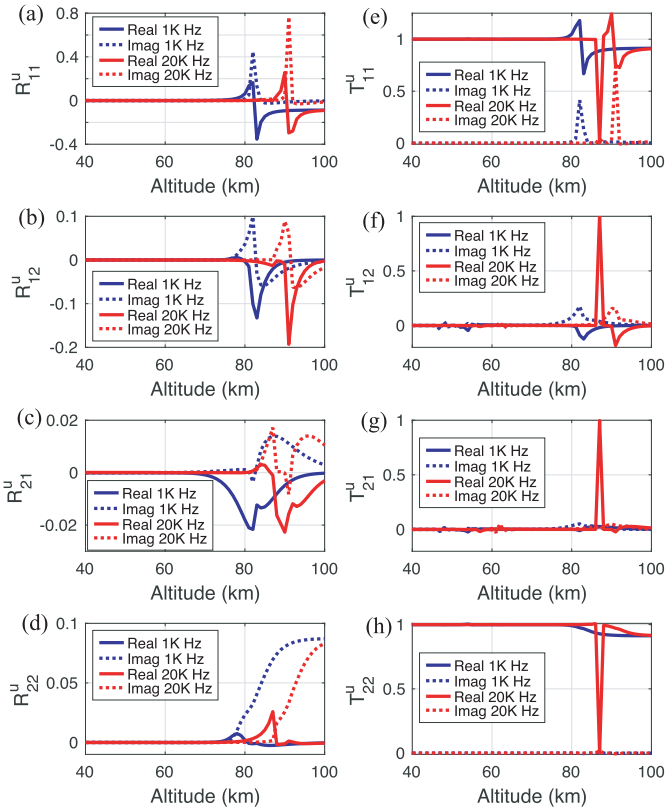

Fig. 5. Variations of reflection and transmission coefficients of upgoing waves in the ionosphere at different altitudes for 1 and 20 kHz plane waves. (a)–(d) Reflection coefficients. (e)–(h) Transmission coefficients.

1) Waves with different frequencies are reflected at different altitudes. The reflection altitude of 20 kHz wave is in the range of 85–95 km, but for the wave at 1 kHz this range falls between 75 and 85 km. This is easy to understand in mathematics since the denominators of (5) increase as the EM wave frequency increases, and this causes the anisotropic dispersive plasma medium gradually degenerating into isotropic air. In physics, the free electron motion in ionosphere cannot follow the EM wave oscillation when the frequency is too high. This is the working principle of ionosonde. A series of frequency sweeping pulses are injected into ionosphere, and echoes for different frequencies occur at different heights.
2) The arbitrary full anisotropy of ionosphere plasma at high altitudes leads to the cross polarization between type I and type II waves, which is shown by R^u_{12} and R^u_{21}. Clearly, below 70 km, there is no cross coupling between these two types of waves since the ionosphere behaves like air for waves with the frequency larger than 1 kHz. When cross coupling occurs at high altitudes, the amplitudes of R^u_{12} and R^u_{21} are smaller than the amplitude of R^u_{11}. The cross coupling in reflection is not dominant. Direct reflection is dominant.

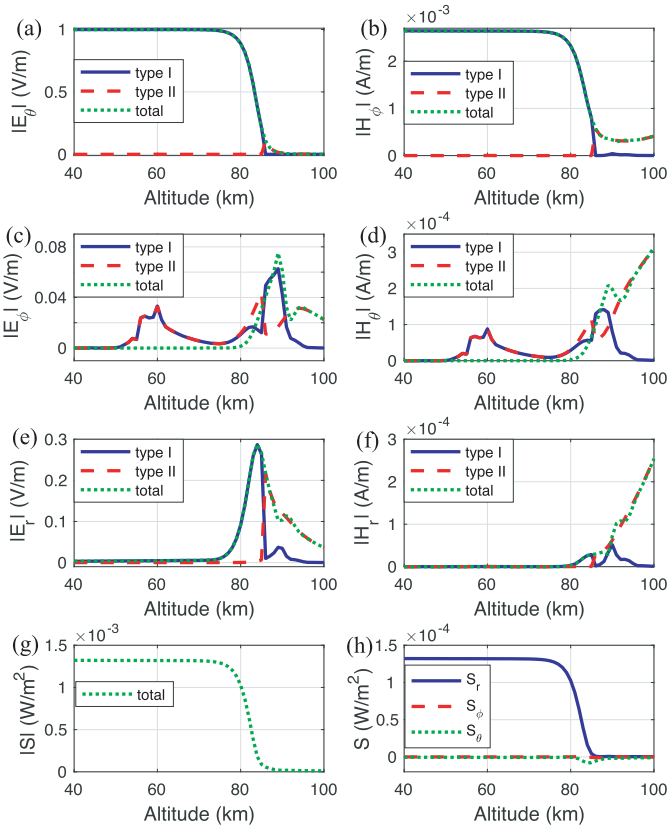

Fig. 6. Variations of EM fields and Poynting vectors for the 20 kHz plane wave. (a)–(f) EM field variations with altitude changes. (g) and (h) Poynting vector variations with altitude changes.

3) R_{22}^u almost becomes a pure imaginary number at high altitudes. The reflected type II wave from itself has a near 90° sudden phase change in the ionosphere. This looks like a total reflection scenario where the reflected wave undergoes a Goos–Hänchen phase shift.
4) At altitudes below 75 km, the transmission coefficients T_{11}^u and T_{22}^u remain constant. The EM waves propagate in the ionosphere like in air. Some fluctuations around horizontal axes show up in the T_{12}^u and T_{21}^u curves for the altitude range between 50 and 75 km. They are actually caused by the uncertainty of numerical computation for type I and type II waves. This can be verified by the EM field value variations which will be discussed next. However, at higher altitudes, above 75 km for 1 kHz and above 85 km for 20 kHz, all four transmission coefficients show obvious variations. The arbitrary full anisotropy of ionosphere leads to the cross coupling between two types of waves, which is consistent with the obvious variations of reflection coefficients.
5) At the altitude 87 km, very sharp peaks show up in all transmission coefficient curves for 20 kHz frequency. This is because the electron density difference between the two adjacent discretized layers becomes larger at high altitudes. The fast change of plasma parameter causes the complete exchange of eigenvalues of two type of waves.

Fig. 6 shows variations of EM fields and Poynting vectors for the 20 kHz plane wave at different altitudes. For convenience, we transform the field variables in the Cartesian coordinate $\hat{x}\hat{y}\hat{z}$ into those in the spherical coordinate $\hat{r}\hat{\theta}\hat{\phi}$ where $\hat{r}$ overlaps with the upgoing wave propagation direction in air. Obviously, below 75 km, only TM wave exists. Although between 50 and 75 km, E_ϕ and H_θ show up for both type I and type II waves, the contribution from two types waves is canceled. The total E_ϕ and H_θ remain zero. This is consistent with the variations of T_{12}^u and T_{21}^u at this altitude range. However, beginning at 75 km, the amplitude of the TM wave decays rapidly and the TE wave shows up. In addition, the EM waves at this altitude range also have the radial components due to the anisotropic ionosphere refraction. The interactions between EM waves and ionosphere are complicated. The EM energy is coupled among different field components. Fig. 6(g) shows the variations of the power density flow of the upgoing waves at different altitudes. Above 80 km, it decays rapidly. At the altitude 100 km, it almost becomes zero. All energy is reflected back to earth or attenuated by ionosphere. Fig. 6(h) shows variations of three components of the Poynting vector. At low altitudes, energy only flows in the $\hat{r}$-direction. But near 85 km, the Poynting vector also has $\hat{\theta}$ and $\hat{\phi}$ components. All three components decay to zero when the altitude approaches 100 km.

B. Radio Sferics Impinge on Ionosphere

In this section, we compare the numerical results simulated by our FDFW model with FDTD results shown in [13, Fig. 6]. We use the same parameters as those in FDTD simulations. The geomagnetic field intensity is set to be 5×10^{-5} T. The inclination is 70°. We let the sferics receiver locate in the northeast of the lightning return stroke and set the declination to be −45°. In this way, the geomagnetic field is perpendicular to the wave propagation direction. The length of the lightning current channel is set as 10 km and the current moment waveform is given in (10). We use the exponential electron density and collision frequency profiles given in (1) and let $h' = 84.2$ km and $\beta = 0.5$ km^{-1}. The distance between the lightning return stroke and sferics receiver is 894 km. The relative permittivity of ground is set to be 10 and the conductivity is 0.01 S/m. The discretized layer thickness in our model is 1 km which is the same as the grid size in the FDTD model.

Fig. 7 shows the comparisons of sferics spectra between FDTD simulations and FDFW model computation with or without the EFT applied. FDTD results are the Fourier transforms of time-domain waveforms. For our FDFW model computation, we totally choose 200 sampling frequencies uniformly distributed from 100 Hz to 20 kHz with the step 100 Hz. Between 20 and 30 kHz, we increase the step to 500 Hz since the spectrum curves from FDTD become smoother. In addition, the spectra are normalized by their maximum amplitudes. We can see the spectra computed by FDTD and FDFW models match well in the whole VLF band, no matter with or without earth curvature compensation. Obviously, the earth curvature mainly affects the spectrum in the high-frequency band. In [13], it is concluded that earth curvature has little effect on the simulated spectrum when

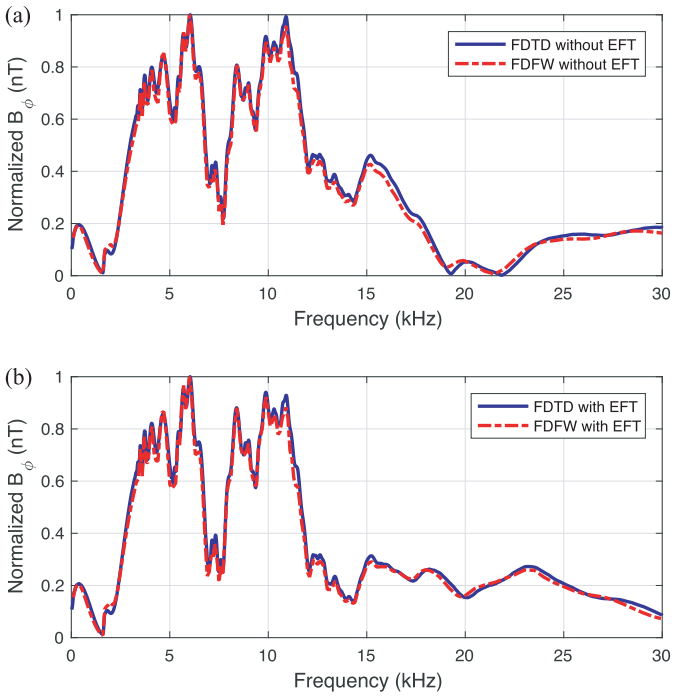

Fig. 7. Comparisons between FDTD simulated results shown in [13, Fig. 6] and our FDFW model computation. (a) Earth curvature is not compensated. (b) Earth curvature is compensated by EFT.

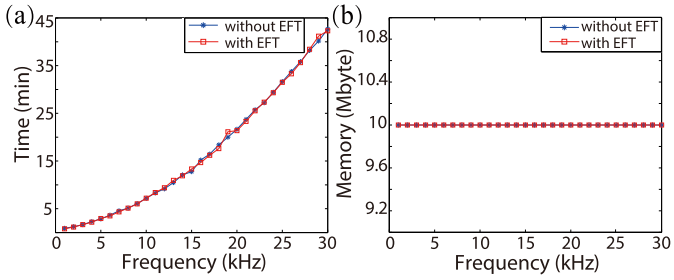

Fig. 8. Computation cost of the FDFW model for the numerical example shown in [13, Fig. 6]. (a) Time consumption for different frequencies. (b) Memory consumption for different frequencies.

the frequency is lower than 12 kHz. Intuitively, this is as we expected. The EFT is realized by modifying the refractive index or **k** vector in each discretized layer. Lower frequency waves undergo fewer field variations in each layer, and thus the EFT changes the field values little.

Then, we analyze the computation cost of FDFW model for the numerical example in [13]. The sferics propagation distance is 894 km, and the bandwidth is 30 kHz. We choose 30 discrete frequencies and record the consumption of time and memory. The program is run in a workstation with 20-cores Xeon E2650 v3 2.3 G CPU, 512 GB RAM. However, for each frequency, FDFW is implemented independently by only one CPU core. Fig. 8 shows the consumption of time and memory for different frequencies. We can see that the computation time increases with the frequency increases while the memory cost remains unchanged. The cost for the FDFW with or without EFT is almost the same. When the frequency becomes larger, k_{px} in Fig. 2 also becomes larger. The integration path becomes longer and the computation time increases. However, because the 2-D integration in (8) is realized by arithmetic accumulation of the sampling values of the integrands in the k_x-k_y plane, the memory consumption is negligible and keeps unchanged when k_{px} increases. For the compensation of earth curvature effects, only the k_x and k_y are adjusted slightly by the EFT. It has little effect on the computation cost. Because no computation time information is given in [13], we cannot directly compare the efficiency of FDTD and FDFW. Fortunately, in [21], the simulation time of FDTD for several numerical experiments is provided although the computation configurations, e.g., propagation distance, ionosphere parameters, CPU speed etc., are different from those in our FDFW model. We can roughly compare the computation time of FDTD and FDFW. We take the results and time information shown in [21, Fig. 5] and compare them with our FDFW simulation because the top of the computation domain in our FDFW model is also at the altitude of 100 km. The FDFW model needs around 21 min to accomplish the computation of 20 kHz wavefields at the observation point. However, the explicit FDTD model needs around 11 min while the implicit model only needs 3 min with a 3.0 G CPU. One reason for the fast computation of FDTD in [21] is the moving domain technique which actually helps to compress the large whole computation domain into a small local domain only containing the band-limited non-null sferics pulse. Consequently, computation time is significantly saved. Unfortunately, the moving domain is a time-domain technique and cannot be applied to our FDFW model. Another aspect for which the FDTD outperforms FDFW is the simulation of broadband sferics. FDFW needs to sweep the sampling frequencies. By contrast, we can obtain the whole sferics waveform through implementing the FDTD only once. However, as we emphasized in Section I, the motivation for developing the FDFW model is not to simulate the sferics propagation in a very fast way but to combine it with a frequency domain inverse model in the future. And in an inverse model, only a limited number of sampling frequencies are used [29] and there is no need to evaluate the intact time-domain waveform. On the other hand, because FDFW is carried out independently for each frequency, it is straightforward to perform the parallel computation in a machine with multiple CPU cores. In addition, it is also not difficult to compute the 2-D numerical integration in (8) in a parallel way. With these techniques, in one iteration of the inverse model, the forward FDFW computation probably can be accomplished in less than 10 min with several hundred megabytes memory consumption. Such cost is affordable for a normal inverse model and can be used to reconstruct the anisotropic ionosphere parameters in the future.

IV. Field Measurements Validations

We further verify the FDFW model by comparing the simulated results with field measured data. The magnetic flux densities B_ϕ of the sferics excited by several lightning return strokes are recorded by the VLF/ELF receiver locating near Duke University. The data are shown in [13, Fig. 7]. The lightning strokes occur in local nighttime and in the southeast of the receiver with the azimuth angle 280°. Since most

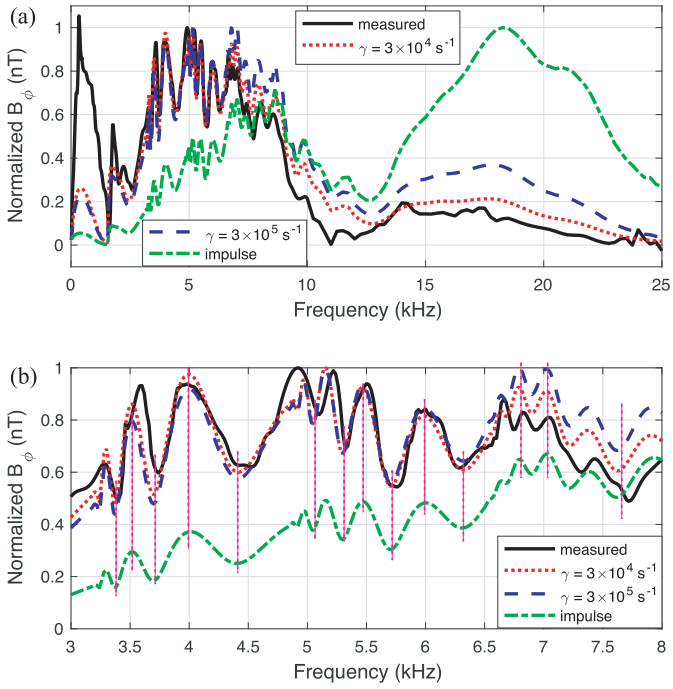

Fig. 9. Comparisons between field measured sferics spectrum shown in [13, Fig. 7] and our FDFW model computation. Different lightning current waveforms are used in FDFW simulation. (a) Spectra in the frequency band 0–25 kHz. (b) Spectra in the frequency band 3–8 kHz.

propagation path is in the seawater, the ground relative permittivity and the conductivity are set to be 81 and 4 S/m, respectively. For the ionosphere parameters, we choose $h' = 85.6$ km and $\beta = 0.45$ km^{-1}. Fig. 9 shows the comparisons between recorded B_ϕ and FDFW model computation results when different lightning current models are used. We adjust the controlling parameters of the doubly exponential expression in (10) and investigate how the lightning current waveform affects the sferics spectra. The parameter γ is set as 3×10^4 s^{-1} and 3×10^5 s^{-1}, respectively. In addition, we also compare the impulse response of EIWG with the measured sferics spectrum. In FDFW computation, impulse responses are actually first computed for sampling frequencies and then the spectrum of the lightning current is multiplied with them to obtain the broadband sferics spectra. It should be noted that the magnetic field receiver response and electronic circuit filters are applied to the FDFW simulated results shown Fig. 9 when $\gamma = 3 \times 10^4$ s^{-1} and 3×10^5 s^{-1}.

We can see that the FDFW model computation results match the measured spectrum well in the range 3–6.5 kHz. In the ELF range below 1.5 kHz there is big peak in the measured spectrum. However, in the simulated results, the magnitude is rather low. Above 10 kHz, the computed spectrum for $\gamma = 3 \times 10^4$ s^{-1} matches the measured better compared with $\gamma = 3 \times 10^5$ s^{-1}. The magnitude of the spectrum for $\gamma = 3 \times 10^5$ s^{-1} is larger than that for $\gamma = 3 \times 10^4$ s^{-1}. This is caused by the energy distribution in the lightning current waveform. When γ becomes larger, the time domain waveform given in (10) decays slower. The higher frequency band energy increases relatively. This is more obviously shown by the EIWG impulse response. Since the impulse response is generated by a time-domain delta waveform having an infinitely flat frequency spectrum, the energy of the sferics spectrum in the range of 12–25 kHz is rather large.

The above analysis implies that the lightning current waveform has a significant effect on the sferics spectra. On the other hand, one should note that the "peak" and "valley" positions in the spectrum curves do not change when the lightning current waveform varies, as is shown in Fig. 9(b). This is as we expected. If the ionosphere is absent, the observed spectrum of the EM wave excited by a lightning return stroke should be smooth. When ionosphere is present, the EIWG forms. The broadband sferics propagate inside it. Different frequency components have different behaviors. Some waves are cutoff, some waves have high attenuation, but some can propagate with low attenuation. Different waveguide modes interfere with each other, and thus the "peak" and "valley" patterns generate. Therefore, these "peak" and "valley" patterns are only related to ionosphere parameters and have no relationship with the lightning current waveform. Numerical simulations show that larger h' causes the "peak" and "valley" patterns shifting to lower frequency ranges. This has been discussed in [41] and will not be repeated here.

V. Conclusion

In this article, a new frequency-domain numerical model is developed to calculate the sferics propagation in EIWG, which has the potential application for ionospheric D region remote sensing. Different from the previous FDTD model in which the anisotropy of the magnetized cold plasma is taken into account by coupling the Lorentz current equations for charged particles into Maxwell's equations, we directly compute the arbitrary anisotropic dielectric constant of the magnetized cold plasma. The wavefields at the sferics receivers are evaluated through plane wave decomposition, computation of reflection and transmission matrices in layered ionosphere, 2-D numerical integration, and compensation for earth curvature effects by EFT.

Compared with the traditional FDTD model, the FDFW model proposed in this article has no advantage of computation speed. But it has two merits. First, because the dielectric permittivity of the magnetized plasma of ionosphere is directly manifested in the mathematical system of the FDFW model, it is convenient to study the interactions between plane waves and ionosphere. Simulation results show that higher frequency waves have higher reflection altitudes. We also notice the strong coupling between type I and type II waves, or between TE and TM waves in the anisotropic ionosphere. The power decay trends of upgoing waves inside the high-altitude ionosphere indicate that most VLF energy of sferics are reflected back at D region altitudes and thus they can be used for D region remote sensing. Another merit of the FDFW is that it can be easily combined with an inverse model to reconstruct the anisotropic ionosphere parameters in each discretized layer. Because the anisotropic complex permittivity of each layer explicitly shows up in the mathematical formulas of the FDFW model, it is possible to construct an L2 norm cost function with the anisotropic

ionosphere parameters explicitly detached which facilitates an iteration solution for the inversion of these parameters.

To further validate the proposed FDFW model, we compare the sferics spectra computed by FDFW with both FDTD simulations and field measured data presented in literatures. Comparisons with the FDTD computation show that the sferics spectra match well almost in the whole ELF/VLF band with or without the EFT applied for earth curvature compensation. Comparisons with field measured data show that both the lightning current waveforms and ionosphere parameters have obvious effects on sferics spectra. The lightning current waveform decides the relative energy distribution of sferics in the VLF/ELF band, i.e., the slow varying trend of the spectrum curve. On the other hand, the ionosphere parameters decide the "peak" and "valley" patterns in the spectrum curve. These observations imply that directly matching a measured spectrum with a best fitted simulated spectrum with the minimum fitting error to infer the D region parameters is not feasible since the lightning current also plays a role for the spectrum fitting. It is desirable to remove the lightning current effect and find the EIWG impulse response before reconstructing the ionosphere parameters. One possible solution for extracting the lightning current spectrum is to make use of the ground wave pulse contained in the sferics waveform. In the time domain, the sferics are composed of a series of pulses [42]. The first pulse is called ground wave. It is the direct wave from the lightning return stroke, and has no relationship with ionosphere. However, how to extract the lightning spectrum will be discussed in our future work.

The FDFW model proposed in this article only works for earth mid- and low-latitude regions where the ambient geomagnetic field is almost homogeneous across the sferics propagation path. This is quite different from previous FDTD model since FDFW model is based on wave propagation in layered anisotropic media. A horizontally heterogeneous medium is not supported in the current FDFW model. In our next article, we will focus on the inverse modeling, i.e., we assume the sferics are already measured and infer the D region parameters.

REFERENCES

[1] S. A. Cummer, U. S. Inan, and T. F. Bell, "Ionospheric D region remote sensing using VLF radio atmospherics," *Radio Sci.*, vol. 33, no. 6, pp. 1781–1792, 1998.

[2] W. L. Taylor, "VLF attenuation for east-west and west-east daytime propagation using atmospherics," *J. Geophys. Res.*, vol. 65, no. 7, pp. 1933–1938, 1960.

[3] L. J. Nickisch and P. M. Franke, "Finite-difference time-domain solution of Maxwell's equations for the dispersive ionosphere," *IEEE Antennas Propag. Mag.*, vol. 34, no. 5, pp. 33–39, Oct. 1992.

[4] J. L. Young, "A higher order FDTD method for EM propagation in a collisionless cold plasma," *IEEE Trans. Antennas Propag.*, vol. 44, no. 9, pp. 1283–1289, Sep. 1996.

[5] T. Kashiwa, N. Yoshida, and I. Fukai, "Transient analysis of a magnetized plasma in three-dimensional space," *IEEE Trans. Antennas Propag.*, vol. AP-36, no. 8, pp. 1096–1105, Aug. 1988.

[6] R. J. Luebbers, F. Hunsberger, and K. S. Kunz, "A frequency-dependent finite-difference time-domain formulation for transient propagation in plasma," *IEEE Trans. Antennas Propag.*, vol. 39, no. 1, pp. 29–34, Jan. 1991.

[7] J. L. Young, "A full finite difference time domain implementation for radio wave propagation in a plasma," *Radio Sci.*, vol. 29, no. 6, pp. 1513–1522, 1994.

[8] D. F. Kelley and R. J. Luebbers, "Piecewise linear recursive convolution for dispersive media using FDTD," *IEEE Trans. Antennas Propag.*, vol. 44, no. 6, pp. 792–797, Jun. 1996.

[9] G.-X. Fan and Q. H. Liu, "An FDTD algorithm with perfectly matched layers for general dispersive media," *IEEE Trans. Antennas Propag.*, vol. 48, no. 5, pp. 637–646, May 2000.

[10] S. A. Cummer, "An analysis of new and existing FDTD methods for isotropic cold plasma and a method for improving their accuracy," *IEEE Trans. Antennas Propag.*, vol. 45, no. 3, pp. 392–400, Mar. 1997.

[11] F. Hunsberger, R. Luebbers, and K. Kunz, "Finite-difference time-domain analysis of gyrotropic media. I. Magnetized plasma," *IEEE Trans. Antennas Propag.*, vol. 40, no. 12, pp. 1489–1495, Dec. 1992.

[12] S. A. Cummer, "Modeling electromagnetic propagation in the earth-ionosphere waveguide," *IEEE Trans. Antennas Propag.*, vol. 48, no. 9, pp. 1420–1429, Sep. 2000.

[13] W. Hu and S. A. Cummer, "An FDTD model for low and high altitude lightning-generated EM fields," *IEEE Trans. Antennas Propag.*, vol. 54, no. 5, pp. 1513–1522, May 2006.

[14] Y. Yu and J. J. Simpson, "An E-J collocated 3-D FDTD model of electromagnetic wave propagation in magnetized cold plasma," *IEEE Trans. Antennas Propag.*, vol. 58, no. 2, pp. 469–478, Feb. 2010.

[15] Y. Yu, J. Niu, and J. J. Simpson, "A 3-D global earth-ionosphere FDTD model including an anisotropic magnetized plasma ionosphere," *IEEE Trans. Antennas Propag.*, vol. 60, no. 7, pp. 3246–3256, Jul. 2012.

[16] B. T. Nguyen, C. Furse, and J. J. Simpson, "A 3-D stochastic FDTD model of electromagnetic wave propagation in magnetized ionosphere plasma," *IEEE Trans. Antennas Propag.*, vol. 63, no. 1, pp. 304–313, Jan. 2015.

[17] B. T. Nguyen, A. Samimi, S. E. W. Vergara, C. D. Sarris, and J. J. Simpson, "Analysis of electromagnetic wave propagation in variable magnetized plasma via polynomial chaos expansion," *IEEE Trans. Antennas Propag.*, vol. 67, no. 1, pp. 438–449, Jan. 2019.

[18] M. Thévenot, J.-P. Bérenger, T. Monedière, and F. Jecko, "A FDTD scheme for the computation of VLF-LF propagation in the anisotropic earth-ionosphere waveguide," *Ann. Télécommun.*, vol. 54, nos. 5–6, pp. 297–310, 1999.

[19] J.-P. Bérenger, "FDTD computation of VLF-LF propagation in the earth-ionosphere waveguide," *Ann. Télécommun.*, vol. 57, nos. 11–12, pp. 1059–1090, 2002.

[20] J.-P. Bérenger, "Long range propagation of lightning pulses using the FDTD method," *IEEE Trans. Electromagn. Compat.*, vol. 47, no. 4, pp. 1008–1011, Nov. 2005.

[21] J.-P. Bérenger, "An implicit FDTD scheme for the propagation of VLF–LF radio waves in the earth–ionosphere waveguide," *Comp. Rendus Phys.*, vol. 15, pp. 393–402, May 2014.

[22] Z. Ma, C. L. Croskey, and L. C. Hale, "The electrodynamic responses of the atmosphere and ionosphere to the lightning discharge," *J. Atmos. Sol.-Terr. Phys.*, vol. 60, pp. 845–861, May 1998.

[23] C. Yang and B. Zhou, "Calculation methods of electromagnetic fields very close to lightning," *IEEE Trans. Electromagn. Compat.*, vol. 46, no. 1, pp. 133–141, Feb. 2004.

[24] J. A. Ferguson, F. P. Snyder, D. G. Morfitt, and C. H. Shellman, *Longwave Propagation Capability and Documentation*, document 1518, Naval Ocean Systems Center, San Diego, CA, USA, 1989.

[25] K. G. Budden, *The Wave-Guide Mode Theory of Wave Propagation*. London, U.K.: Logos Press, 1961.

[26] R. A. Pappert and J. A. Ferguson, "VLF/LF mode conversion model calculations for air to air transmissions in the earth-ionosphere waveguide," *Radio Sci.*, vol. 21, no. 4, pp. 551–558, 1986.

[27] S. A. Cummer and U. S. Inan, "Modeling ELF radio atmospheric propagation and extracting lightning currents from ELF observations," *Radio Sci.*, vol. 35, no. 2, pp. 385–394, 2000.

[28] R. A. Marshall, T. Wallace, and M. Turbe, "Finite-difference modeling of very-low-frequency propagation in the earth-ionosphere waveguide," *IEEE Trans. Antennas Propagat.*, vol. 65, no. 15, pp. 7185–7197, Dec. 2017.

[29] B. Liang *et al.*, "A new inversion method based on distorted born iterative method for grounded electrical source airborne transient electromagnetics," *IEEE Trans. Geosci. Remote Sens.*, vol. 56, no. 2, pp. 877–887, Feb. 2018.

[30] J. R. Wait and K. P. Spies, *Characteristics of the Earth-Ionosphere Waveguide for VLF Radio Waves*. Boulder, CO, USA: National Bureau of Standards, 1964.

[31] Z. Cheng, S. A. Cummer, D. N. Baker, and S. G. Kanekal, "Nighttime *D* region electron density profiles and variabilities inferred from broadband measurements using VLF radio emissions from lightning," *J. Geophys. Res.*, vol. 111, May 2006, Art. no. A05302.
[32] V. P. Pasko, U. S. Inan, and T. F. Bell, "Mesospheric electric field transients due to tropospheric lightning discharges," *Geophys. Res. Lett.*, vol. 26, no. 9, pp. 1247–1250, May 1999.
[33] Y. Hu, Y. Fang, D. Wang, Y. Zhong, and Q. H. Liu, "Electromagnetic waves in multilayered generalized anisotropic media," *IEEE Trans. Geosci. Remote Sens.*, vol. 56, no. 10, pp. 5758–5766, Oct. 2018.
[34] K. Sainath, F. L. Teixeira, and B. Donderici, "Robust computation of dipole electromagnetic fields in arbitrarily anisotropic, planar-stratified environments," *Phys. Rev. E, Stat. Phys. Plasmas Fluids Relat. Interdiscip. Top.*, vol. 89, Jan. 2014, Art. no. 013312.
[35] K. A. Michalski, "Extrapolation methods for Sommerfeld integral tails," *IEEE Trans. Antennas Propag.*, vol. 46, no. 10, pp. 1405–1418, Oct. 1998.
[36] D. L. Jones, "Electromagnetic radiation from multiple return strokes of lightning," *J. Atmos. Terr. Phys.*, vol. 32, pp. 1077–1093, Jun. 1970.
[37] A. S. Dennis and E. T. Pierce, "The return stroke of the lightning flash to earth as a source of VLF atmospherics," *Radio Sci.*, vol. 68D, pp. 777–794, 1967.
[38] V. A. Rakov and M. A. Uman, *Lightning: Physics and Effects*. Cambridge, U.K.: Cambridge Univ. Press, 2003.
[39] Y.-L. Geng, X.-B. Wu, L.-W. Li, and B.-R. Guan, "Electromagnetic scattering by an inhomogeneous plasma anisotropic sphere of multilayers," *IEEE Trans. Antennas Propag.*, vol. 53, no. 12, pp. 3982–3989, Dec. 2005.
[40] K. G. Budden, *The Propagation of Radio Waves: The Theory of Radio Waves of Low Power in the Ionosphere and Magnetosphere*. New York, NY, USA: Cambridge Univ. Press, 1985, pp. 143, 260, and 564–565.
[41] F. Han and S. A. Cummer, "Midlatitude nighttime D region ionosphere variability on hourly to monthly time scales," *J. Geophys. Res.*, vol. 115, no. A9, 2010, Art. no. A09323.
[42] F. Han, "Midlatitude *D* region variations measured from broadband radio atmospherics," Ph.D. dissertation, Dept. Elect. Comput. Eng., Duke Univ., Durham, NC, USA, 2011.

Feng Han (M'17) received the B.S. degree in electronic science from Beijing Normal University, Beijing, China, in 2003, the M.S. degree in geophysics from Peking University, Beijing, in 2006, and the Ph.D. degree in electrical engineering from Duke University, Durham, NC, USA, in 2011.

He is currently an Assistant Professor with the Institute of Electromagnetics and Acoustics, Xiamen University, Xiamen, China. His research interests include ionosphere remote sensing by radio atmospherics, electromagnetic full-wave inversion by integral equations, reverse time migration image, and the design of an electromagnetic detection system.

Bingyang Liang received the B.E. degree in communication engineering from PLA Information Engineering University, Zhengzhou, China, in 2011, and the M.S. degree in electronics and communication engineering and the Ph.D. degree in electronic science from Xiamen University, Xiamen, China, in 2014 and 2019, respectively.

His research interests include the forward and inversion method of electromagnetics and acoustics, as well as their applications in ATEM and photoacoustic tomography.

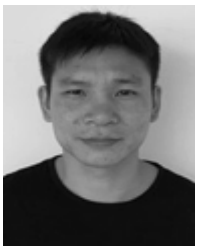

Jiawen Li received the B.S. and M.S. degrees in electronic science and technology from the Wuhan University of Technology of China, Wuhan, China, in 2011 and 2016, respectively. He is currently pursuing the Ph.D. degree with Xiamen University, Xiamen, China.

His research interests include electromagnetic scattering and inverse scattering in complex media and the full-wave inversion of anisotropic targets.

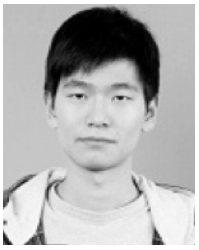

Feifan Liu received the B.E. degree in software engineering from Northwestern Polytechnical University, Xi'an, China, in 2014. He is currently pursuing the Ph.D. degree with the University of Science and Technology of China, Hefei, China.

His research interests include electrical discharges in earth's atmosphere, such as narrow bipolar events, jets, and their effects on near-earth space environment. He has also participated in the setup of local lightning detection network Jianghuai Area Sferic Array (JASA), and is now responsible for the routine maintenance and data analysis.

Gaopeng Lu received the B.S. degree in atmospheric physics from the University of Science and Technology of China (USTC), Hefei, China, in 2003, and the Ph.D. degree in physics from the New Mexico Institute of Mining and Technology, Socorro, NM, USA, in 2008.

He is currently a Full-Time Professor with the School of Earth and Space Sciences, USTC. His main research interests include the charge transfer in lightning and the associated lightning effects, such as transient luminous events, terrestrial gamma-ray flashes, and lightning-induced hazards.

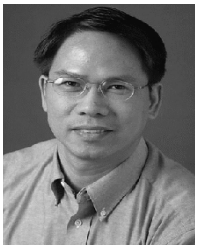

Qing Huo Liu (S'88–M'89–SM'94–F'05) received the B.S. and M.S. degrees in physics from Xiamen University, Xiamen, China, in 1983 and 1986, respectively, and the Ph.D. degree in electrical engineering from the University of Illinois at Urbana–Champaign, IL, USA, in 1989.

He was with the Electromagnetics Laboratory, University of Illinois at Urbana–Champaign, as a Research Assistant from September 1986 to December 1988, and as a Post-Doctoral Research Associate from January 1989 to February 1990. He was a Research Scientist and Program Leader with Schlumberger-Doll Research, Ridgefield, CT, USA, from 1990 to 1995. From 1996 to May 1999, he was an Associate Professor with New Mexico State University, Las Cruces, NM, USA. Since June 1999, he has been with Duke University, where he is currently a Professor of electrical and computer engineering. He has published over 400 articles in refereed journals and 500 articles in conference proceedings. His research interests include computational electromagnetics and acoustics, inverse problems, and their application in nanophotonics, geophysics, biomedical imaging, and electronic packaging.

Dr. Liu is a fellow of the Acoustical Society of America, the Electromagnetics Academy, and the Optical Society of America. He currently serves as the founding Editor-in-Chief for the new IEEE JOURNAL ON MULTISCALE AND MULTIPHYSICS COMPUTATIONAL TECHNIQUES, the Deputy Editor-in-Chief of *Progress in Electromagnetics Research*, an Associate Editor for the IEEE TRANSACTIONS ON GEOSCIENCE AND REMOTE SENSING, and an Editor of the *Journal of Computational Acoustics*.